

# Thermo-Electrochemical Redox Flow Battery for Continuous Conversion of Low-Grade Waste Heat to Power

**Jorrit Bleeker**

Delft University of Technology

**Stijn Reichert**

Delft University of Technology

**Joost Veerman**

REDstack

**David Vermaas** (✉ [d.a.vermaas@tudelft.nl](mailto:d.a.vermaas@tudelft.nl))

Delft University of Technology

---

## Research Article

**Keywords:** temperature dependency, Seebeck effect, fluid-based redox-active species, Carnot, heat exchangers

**Posted Date:** January 3rd, 2022

**DOI:** <https://doi.org/10.21203/rs.3.rs-1196162/v1>

**License:**  This work is licensed under a Creative Commons Attribution 4.0 International License.

[Read Full License](#)

---

# 1 Thermo-electrochemical redox flow battery for continuous conversion of low- 2 grade waste heat to power

3 Jorrit Bleeker <sup>1</sup>, Stijn Reichert <sup>1</sup>, Joost Veerman <sup>2</sup>, David A. Vermaas <sup>1,\*</sup>

4 <sup>1</sup>Department of Chemical Engineering, Delft University of Technology, 2629 HZ Delft, The  
5 Netherlands

6 <sup>2</sup>REDstack, Graaf Adolfstraat 35-G, 8606 BT Sneek, The Netherlands

7 email: [d.a.vermaas@tudelft.nl](mailto:d.a.vermaas@tudelft.nl)

8

## 9 **Abstract**

10 Here we assess the route to convert low grade waste heat (<100 °C) into electricity by leveraging the  
11 temperature dependency of redox potentials (Seebeck effect). We use fluid-based redox-active  
12 species, which can be easily heated and cooled using heat exchangers. By using a first principles  
13 approach, we designed a redox flow battery system with  $\text{Fe}(\text{CN})_6^{3-}/\text{Fe}(\text{CN})_6^{4-}$  and  $\text{I}^-/\text{I}_3^-$  chemistry. We  
14 evaluate the continuous operation with one flow cell at high temperature and one at low temperature.  
15 We show that the most sensitive parameter, the Seebeck coefficient, can be controlled via the redox  
16 chemistry, the reaction quotient and solvent additives, and we present the highest Seebeck coefficient  
17 for this RFB chemistry. A power density of 0.6 W/m<sup>2</sup> and stable operation for 2 hours are achieved  
18 experimentally. We predict high (close to Carnot) heat-to-power efficiencies if challenges in the heat  
19 recuperation and Ohmic resistance are overcome, and the Seebeck coefficient is further increased.

20

## 21 **Highlights**

- 22 - We present a proof of concept for stable, continuous thermo-electrochemical heat-to-power  
23 conversion with redox flow batteries
- 24 - A iodide - hexacyanoferrate redox flow battery with a Seebeck coefficient of +2.88 mV/K
- 25 - The Seebeck coefficient is not only controlled by the chemistry, but also substantially impacted  
26 by the reaction quotient and solvent
- 27 - Fitted simulations show that more than 6% of the thermal energy can be converted into  
28 electrical power in batch mode at 80 °C / 20 °C and 90% heat recuperation
- 29 - Further improving the energy efficiency is possible via increasing the Seebeck coefficient (e.g.  
30 mixing solvents)

31

## 32 Introduction

33 In the quest for reducing CO<sub>2</sub> emissions, cutting energy losses has received major attention in the past  
34 decade. Despite various efforts to make industrial and power generating processes more efficient, 50  
35 to 80% of the primary energy is dissipated as waste heat, where low-grade waste heat (up to 100 °C)  
36 forms the largest contribution<sup>1</sup>. Forman *et al* estimated that in 2012 around 43 PWh (1.6·10<sup>20</sup>J) of low-  
37 grade waste heat was emitted globally<sup>1</sup>. Although not all waste heat can be converted into power due  
38 to the conservation of entropy, the Carnot efficiency ( $1 - \frac{T_{hot}}{T_{cold}}$ ) still allows to capture 20% of the low-  
39 grade waste heat (100 °C) as power, assuming an environment of 25 °C. Converting just this fraction  
40 of the low-grade waste heat into electricity could already generate 39% of the world's electricity  
41 consumption (22.3 PWh/year, IEA as of 2018<sup>2</sup>).

42 A major bottleneck for converting low-grade waste heat into power is the low practical efficiency of  
43 existing technologies, even compared to the Carnot efficiency. Traditionally, the organic Rankine cycle  
44 (ORC) has been used, which converts typically 4-9% of the (100-120 °C) waste heat to power<sup>3</sup>. The  
45 relatively low energy efficiency and the corresponding low (environmental and economic) benefits,  
46 have limited the practical application of ORC. Newer heat-to-power technologies, e.g. Reverse  
47 Electrodialysis<sup>4, 5, 6</sup>, Thermal Regenerable redox-flow Batteries<sup>7, 8</sup> or Pressure Retarded Osmosis  
48 combined with membrane distillation<sup>9,10</sup>, have not shown higher energy efficiencies. Hence, a heat-  
49 to-power technology with potential for high energy efficiency is demanded.

50 A recent technology with high potential for efficient conversion is the Thermally Regenerative  
51 Electrochemical Cycle (TREC)<sup>11</sup>, which makes use of the temperature-dependent battery voltage (i.e.,  
52 the Seebeck effect). More energy can be obtained upon discharging at a first temperature, compared  
53 to the charging at a different temperature, generating net electrical power. Lee *et al.* has shown  
54 experimentally, using a solid Cu/Cu hexacyanoferrate (HCF) battery, that waste heat could be  
55 converted into power highly efficiently: even up to 80% of the Carnot efficiency can be reached when  
56 heat would be fully recuperated with a heat exchanger. The work by Lee *et al.* inspired the  
57 development of the TREC over the past years<sup>12</sup>, including a membrane free system (NiHCF, Ag/AgCl)<sup>13</sup>,  
58 a CoHCF based TREC (CoHFC, Ag/AgCl)<sup>14</sup> and even first applications of a TREC into a combustion  
59 engine<sup>15</sup> and the hot roof of a building<sup>16</sup>.

60 However, a practical drawback of the above TRECs is the slow heat transport in solids and stationary  
61 fluids. Hence, the use of a battery based on solid redox active species makes the heat recuperation  
62 unpractical, leading to long cycle times (several hours for Lee *et al.*), corresponding to a low power  
63 density (1.2 mW/g)<sup>11</sup>. Redox Flow Batteries (RFBs) could leverage the intrinsic facile heating and  
64 cooling of liquid redox active species in heat exchangers, which makes them attractive candidates for

65 the TREC. Several electrolytes have been suggested, such as the All-Vanadium RFB by Reynard *et al*<sup>17</sup>  
66 and a  $V^{2+}/V^{3+}$ ,  $Fe(CN)_6^{3-}/Fe(CN)_6^{4-}$  battery by Poletayev *et al*<sup>18</sup>. However, the All-Vanadium RFB suffers  
67 from chlorine formation and  $V_2O_5$  precipitation at elevated (>60 °C) temperatures, and the electrolytes  
68 selected by Poletayev *et al*. will be difficult to separate with a monopolar ion membrane.

69 Here we present a RFB that has high potential for continuous heat to power conversion. Our RFB is  
70 designed based on hexacyanoferrate and iodide/polyiodide redox couples:



73 We evaluate the potential of this route via the criteria for thermo-electrochemical RFBs, and present  
74 a system for continuous heat to power conversion with a TREC based on RFBs. The same chemistry has  
75 been reported by Qian *et al*. recently<sup>19</sup>, and has shown promise for heat to power recovery. In this  
76 work, we report a higher Seebeck coefficient and power density, by changing the concentrations of  
77 the electrolytes and using a KCl supporting electrolyte.

78

## 79 **Working principle**

### 80 Seebeck effect

81 The concept of the thermo-electrochemical flow cell relies on the dependency of the redox potential  
82 on temperature, as described by the Seebeck effect. This temperature dependency is dominantly due  
83 to changes in entropy between reduced and oxidized species (see SI Note 1). The change in redox  
84 potential is described as:

85  $E_i = E_i^0 + \alpha_i(T - T^0)$  eq. 1

86  $\alpha_i \approx \frac{\Delta S_R}{nF}$  eq. 2

87 In which  $E_i$  is the redox potential (in V) of redox reaction  $i$ ,  $E^0$  is the standard potential (in V),  $\alpha$  is the  
88 Seebeck coefficient (in V/K),  $T$  is the reaction temperature (in K),  $T^0$  is the standard temperature (298  
89 K),  $\Delta S_R$  is the reaction entropy for a reduction reaction,  $n$  is the number of electrons involved and  $F$  is  
90 the Faraday constant (96485 C/mol). The concentration dependency of the Seebeck coefficient can be  
91 described as follows<sup>20</sup>:

92  $\alpha = \alpha_0 - \frac{R}{nF} \ln(Q)$  eq. 3

93 Here  $\alpha_0$  is the Seebeck coefficient at standard concentrations and  $Q$  is the reaction quotient of the  
 94 redox reaction (see SI Note 1 for a derivation and comparison of Seebeck coefficients at different  
 95 concentrations).

### 96 Thermo-electrochemical energy

97 The battery's open circuit voltage, OCV (in V), arises from the potential difference between the redox  
 98 potentials of species 1 and 2, where  $Q$  is the reaction quotient of the cell reaction:

$$99 \quad OCV = E_1^0 - E_2^0 + (\alpha_1 - \alpha_2)(T - T^0) - \frac{RT}{nF} \ln(Q) \quad \text{eq. 4}$$

100 The Seebeck effect can be leveraged when using two batteries: one battery in which both anolyte and  
 101 catholyte operate at a high temperature, and a second battery in which both reactions occur at a low  
 102 temperature. The difference in OCV between the hot battery and the cold battery is:

$$103 \quad OCV_{hot} - OCV_{cold} = (\alpha_1 - \alpha_2)(T_{hot} - T_{cold}) - \frac{RT_{hot}}{nF} \ln(Q_{hot}) + \frac{RT_{cold}}{nF} \ln(Q_{cold})$$

$$104 \quad = \alpha_{cell} \Delta T - \frac{R}{nF} \ln \left( \frac{Q_{hot} T_{hot}}{Q_{cold} T_{cold}} \right) \quad \text{eq. 5}$$

105 In which  $Q_{hot}$  and  $Q_{cold}$  indicate the reaction quotient at the operating conditions of the hot and cold  
 106 battery respectively and  $\alpha_{cell}$  is the Seebeck coefficient of the combined electrolytes. The difference in  
 107 OCV drives an electric current between the hot and the cold battery, which can be used as a power  
 108 source (Fig. 1a). The maximum power that can be extracted from the difference in battery voltage is  
 109 given by the Kirchhoff law (eq. 6), which assumes a constant battery resistance,  $R$  (in  $\Omega \text{ m}^2$ ) and a  
 110 constant cell voltage. The maximum power density  $P_{max}$  (in  $\text{W}/\text{m}^2$ ) is then given by:

$$111 \quad P_{max} = \frac{\left( \alpha_{cell} \Delta T - \frac{R}{nF} \ln \left( \frac{Q_{hot} T_{hot}}{Q_{cold} T_{cold}} \right) \right)^2}{4(R_{hot} + R_{cold})} \quad \text{eq. 6}$$

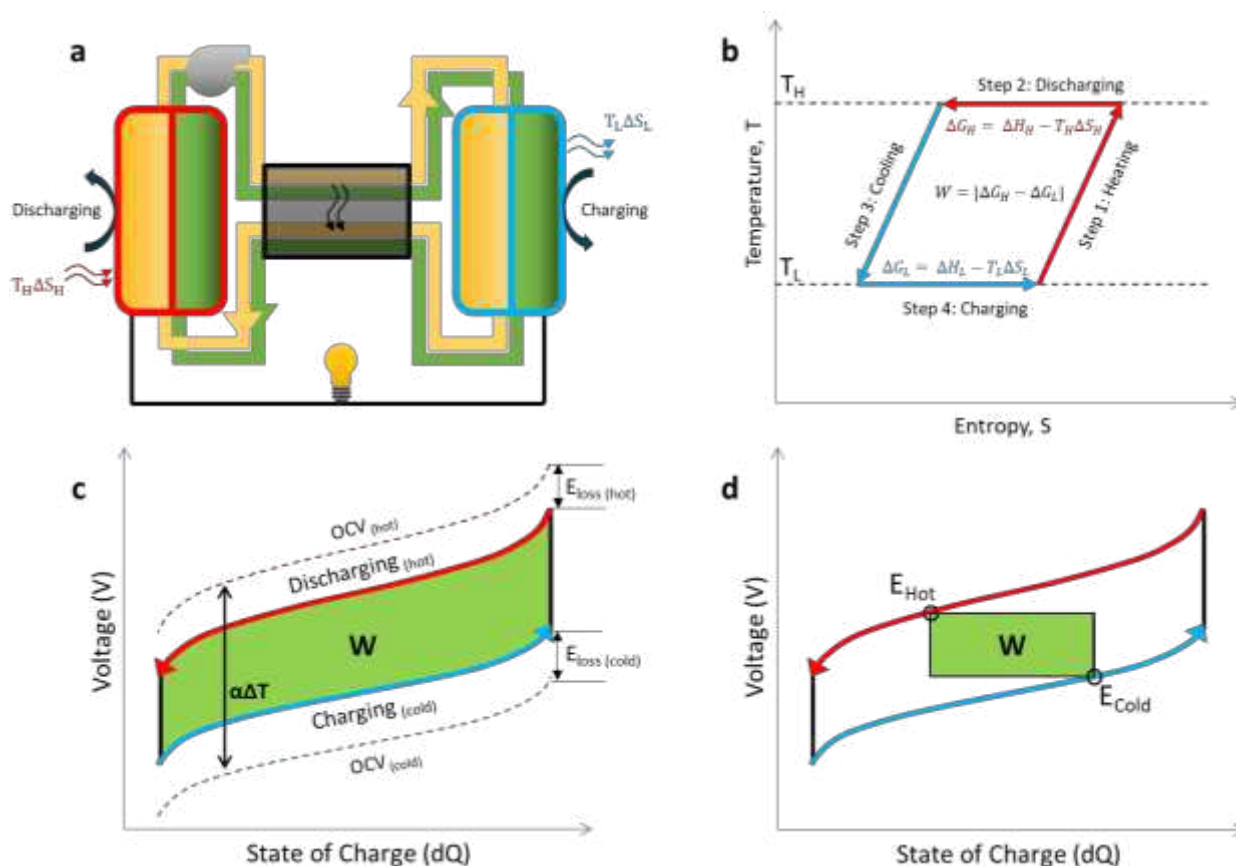
112

### 113 Thermodynamic analysis

114 From a thermodynamic point of view, the battery process can be illustrated in a TS-diagram (Fig. 1b).  
 115 When the heat from the hot RFB outflow is recuperated via a heat exchanger and no losses are  
 116 included, the Carnot efficiency can be obtained (see SI Note 2).

117 The expected voltages at the hot and cold RFB are obtained from eq. 4. When including electrical losses  
 118 (Ohmic resistances, kinetic overpotentials) a V-dQ diagram is established (Fig. 1c&d). The maximum  
 119 work is obtained when the battery voltage is continuously adapted to the individual battery potentials

120 (Fig. 1c). This resembles a batch mode operation, or a segmentation of electrodes that can be  
 121 individually controlled (Fig. S-1). A more practical operation is a continuous, single-stage, battery  
 122 mode. However, this single charge and discharge voltage,  $E_{hot}$  and  $E_{cold}$ , respectively, compromises the  
 123 obtainable work (Fig. 1d).



124  
 125 **Figure 1.** Concept of thermally regenerative redox flow cycle and thermodynamic diagrams. (a) illustrates the  
 126 electrolyte circulation between a hot RFB (red, discharging) and a cold RFB (blue, charging at lower voltage), with  
 127 a heat exchanger in the center. (b). Corresponding  $ST$ -diagram of the charging and discharging cycle. (c). Battery  
 128 voltage as a function of State of Charge, for hot and cold state, indicating the maximum obtainable work ( $W$ ),  
 129 due to Seebeck effect ( $\alpha\Delta T$ ) and including overpotential losses ( $E_{loss}$ ). (d). Battery voltage as a function of State of  
 130 Charge, including the obtainable work when charging and discharging at a single voltage (i.e., continuous mode).

131

## 132 **Methods**

### 133 Materials & electrolyte preparation

134 All chemicals were purchased from commercial suppliers (Alfa Aesar, KGaA, VWR International), and  
 135 were at least of 99% purity and were used without further purification. Demineralized water was used  
 136 to prepare the electrolytes.

137 The Seebeck coefficient of the individual hexacyanoferrate redox couple was measured in 0.1 M  
138  $\text{K}_3\text{Fe}(\text{CN})_6$ , 0.1 M  $\text{K}_4\text{Fe}(\text{CN})_6 \cdot 3\text{H}_2\text{O}$  and 0.3 M KCl. The Seebeck coefficient of the individual polyiodide  
139 redox couple was measured in 0.01 M KI, 0.001 M  $\text{I}_2$ , 1 M KCl. KCl was added to raise the  $\text{K}^+$   
140 concentration to  $\sim 1$  M.

141 The measurement of the cell Seebeck coefficient and the proof of concept were done at higher  
142 concentrations. The hexacyanoferrate electrolyte consisted of 0.3 M  $\text{K}_3\text{Fe}(\text{CN})_6$ , 0.3 M  $\text{K}_4\text{Fe}(\text{CN})_6 \cdot 3\text{H}_2\text{O}$   
143 and 0.35 M KCl. KCl was added in order to obtain 2 M fully dissociated  $\text{K}^+$  ions for all cases. The  
144 polyiodide couple consisted of 0.9 M KI, 0.3 M  $\text{I}_2$  and 1.1 M KCl. The solution was stirred overnight to  
145 dissolve all  $\text{I}_2$ .

#### 146 Individual Seebeck coefficient measurements

147 The Seebeck coefficients were measured by performing cyclic voltammetry at various temperatures  
148 between 20-55 °C in 50 mL of electrolyte on a hotplate stirrer (IKA C-MAG HS7) with two Pt wires as  
149 working and counter electrodes and a Ag/AgCl reference electrode (ProSense, double junction). We  
150 used a custom-made 30 cm long glass salt bridge filled with 1 M KCl (Fig. S-2b) to ensure the Ag/AgCl  
151 reference electrode did not heat up.

152 The cyclic voltammetry was performed using a potentiostat (Ivium CompactStat.h10800) with a scan  
153 rate of 50 mV/s, cycling between -0.2 and 0.5 V vs Ag/AgCl@20 °C for hexacyanoferrate and 0.2 and  
154 0.6 V vs Ag/AgCl@20 °C for polyiodide. The halfway potential ( $E^{1/2}$ ) was calculated by taking the  
155 average of the cathodic and anodic peak positions<sup>21</sup>, which were measured against a Ag/AgCl  
156 reference electrode (ProSense B.V.) at 20 °C. The Seebeck coefficient was taken as the slope of the  
157 linear fit of  $E^{1/2}$  versus T data.

#### 158 Single flow cell characterization

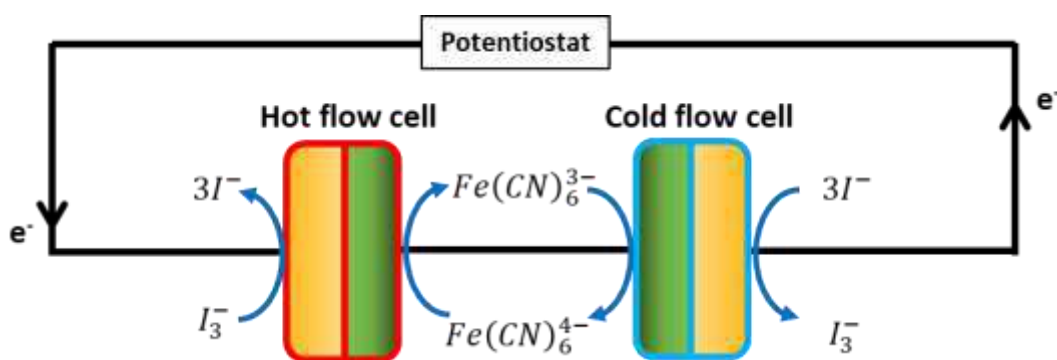
159 The cell Seebeck coefficient (i.e., combined with both redox couples) was experimentally assessed  
160 using a custom-made PTFE flow cell with graphite sheet electrodes with a geometrical surface area of  
161 86.6 cm<sup>2</sup> and FKM gaskets (see Fig. S-4a). The hexacyanoferrate and polyiodide flow compartments  
162 were separated with a Selemion CMV cation exchange membrane. A flow diagram with the various  
163 components can be seen in Fig. S-11. We used 0.5 L of both electrolytes, of which  $\sim 0.25$  L was always  
164 in the system. The Seebeck coefficient was calculated by measuring the open cell voltage (OCV) at  
165 various temperatures between 20-40 °C and performing a linear fit through the data. The OCV was  
166 measured with a potentiostat (IviumStat.h standard). The electrolyte was heated by coiling up part of  
167 the tubing and submerging it in a heating bath (Julabo Corio C-B19). The electrolyte temperature was  
168 measured at the inlet and outlet of the flow cell with four K-type thermocouples (TC Direct - 405-011)  
169 and read out with a NI 9213 module. The OCV was measured once the temperature was stable ( $\pm 0.5$

170 °C for 5 minutes). The temperature of the heating bath was then raised for the next measurement. The  
171 electrolyte was pumped (Masterflex Precision peristaltic pump EW-07528-10) through PTFE tubing,  
172 which was insulated with PE foam. The flow cell was not thermally insulated. The resistance of a single  
173 flow cell was measured with chronopotentiometry, in a range of currents for 60 seconds each (10.3 to  
174  $-10.3 \text{ A/m}^2$ , with increments of  $1.15 \text{ A/m}^2$ ). The resistance was calculated by a linear fit through the  
175 measured voltages.

### 176 Proof of concept measurements

177 A flow diagram of the entire setup can be seen in Fig. S-12. The temperature of the flow cells is  
178 controlled with a cooling bath (Julabo Corio CD-601F), heating bath (Julabo Corio C-B19) and a glass  
179 heat exchanger (custom made by Squall Instruments, 1 m long, 70 double coils, operating in counter-  
180 flow Fig. S-5). The temperature was measured at the inlet and outlet of both flow cells. The operating  
181 temperature of the flow cell was assumed to be the mean outlet temperature of the two electrolytes.

182 The power output of the system was experimentally validated with two flow cells operating at different  
183 temperatures. An electrical loop was made between the two cells and the potentiostat (IviumStat.h  
184 standard), see Fig. 2. A chronopotentiometry method was run at 13 different current densities with  
185 increments of  $1.73 \text{ A/m}^2$  for 60 seconds each. The power density was calculated by multiplying the  
186 current density with the obtained voltage difference over the two cells ( $E_{\text{Cell hot}} - E_{\text{Cell cold}}$ ). Note that the  
187 area in power and current density are for a single flow cell. The system was allowed to run for 3 hours  
188 at the maximum power output to test the stability.



189  
190 *Figure 2: Schematic representation of the electrical connections during the proof of concept measurements. The*  
191 *hot flow cell is discharging (spontaneous reaction), the cold cell is charging (electrolysis).*

### 192 Modelling

193 The heat to power efficiency calculations were performed in a Python script. The used equations and  
194 assumptions are stated in SI Note 6.

195

196 **Results**

197 Selection of suitable redox couples

198 To perform power generation via a thermo-electrochemical RFB in practical heat-to-power  
199 applications, a RFB system should meet the following requirements:

- 200 1. The RFB needs to consist of two solute redox systems with a large difference in Seebeck  
201 coefficients to maximize  $\alpha_{\text{cell}} (= \alpha_1 - \alpha_2)$ .
- 202 2. The redox species need to have a high solubility (allowing small water volume heating/cooling),  
203 fast kinetics (low overpotentials) and stability over a temperature range of at least 10-80 °C  
204 (allowing for high  $\Delta T$ )
- 205 3. All redox active species need to have the same valence sign, to allow separation with a  
206 (monopolar) ion-exchange membrane. A bipolar membrane could be used alternatively, but  
207 the current state-of-the-art bipolar membranes would result in unacceptable large energy  
208 losses<sup>22</sup>.

209 The most mature RFB, the all-vanadium RFB, unfortunately does not meet criteria 1 and 2. Both the  
210 V(II)/(III) and the V(IV)/V(V) couple have positive Seebeck coefficients<sup>23</sup> and the V(V)-ions can  
211 irreversibly precipitate above 40 °C<sup>24</sup>. This could be solved by with a mixed acid electrolytes, however  
212 that can result in Cl<sub>2</sub> gas formation at 60 °C<sup>17</sup>. Also Br<sub>2</sub>-based batteries are unsuitable, due to the high  
213 vapour pressure of bromine at elevated temperatures (boiling point is 59 °C at atmospheric pressure).

214 Other examples of RFB based systems targeting heat to power is consisted Cu(NH<sub>3</sub>)<sub>4</sub><sup>2+</sup>/Cu(NH<sub>3</sub>)<sub>2</sub><sup>+</sup> or  
215 V<sup>2+</sup>/V<sup>3+</sup> and Fe(CN)<sub>6</sub><sup>3-</sup>/Fe(CN)<sub>6</sub><sup>4-</sup>. These electrolytes have the highest reported Seebeck coefficients for  
216 TRECs to date (-2.9 mV/K and -3.0 mV/K respectively)<sup>18, 25</sup>, but do not meet the 3<sup>rd</sup> criterion. Hence,  
217 despite the predicted high efficiencies, the system suffered from ion crossover causing precipitation  
218 of Cu<sub>2</sub>Fe(CN)<sub>6</sub> and a high internal resistance. The V<sup>2+</sup>/V<sup>3+</sup>, Fe(CN)<sub>6</sub><sup>3-</sup>/Fe(CN)<sub>6</sub><sup>4-</sup> was not tested for  
219 stability, but will likely suffer from vanadium crossover as the electrolytes are only separated by a  
220 Nafion cation exchange membrane.

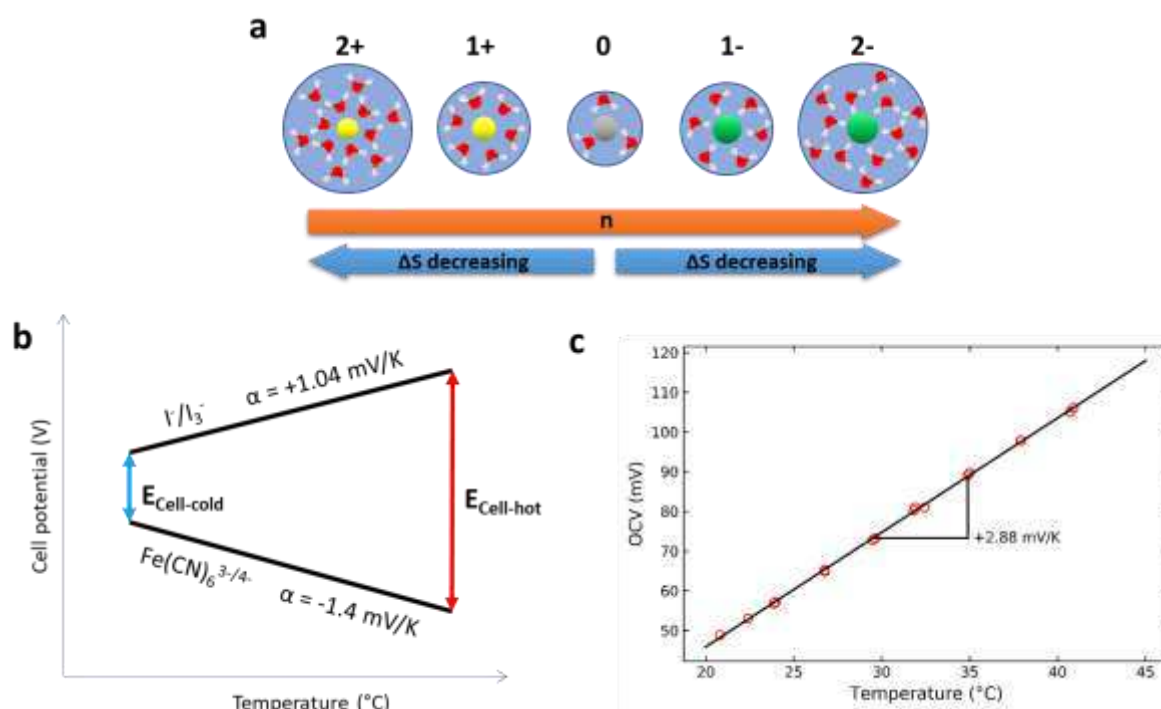
221 The sign of the Seebeck coefficient appears to be correlated with the sign of the valence of the redox  
222 active species that undergo a simple one-electron transfer reaction. For example redox couples  
223 consisting of cations, e.g. Fe<sup>3+</sup>/Fe<sup>2+</sup>, Cu<sup>2+</sup>/Cu<sup>+</sup> and Co<sup>3+</sup>/Co<sup>2+</sup>, all have positive Seebeck coefficients<sup>20, 26</sup>,  
224 while their anion counterparts, e.g. Fe(CN)<sub>6</sub><sup>3-</sup>/Fe(CN)<sub>6</sub><sup>4-</sup> and MnO<sub>4</sub><sup>-</sup>/MnO<sub>4</sub><sup>2-</sup>, have negative coefficients<sup>11</sup>.  
225 <sup>26</sup> (see SI Note 3 for 54 examples from literature sources). We hypothesize that the change in entropy  
226 (and thus the Seebeck coefficient) is dominated by the size of the ion hydration shell, which grows

227 upon increased valence magnitude (Fig. 3a). Unfortunately, this property makes it difficult to satisfy  
 228 both criterion 1 and 3.

229 To match all three criteria we chose the polyiodide redox couple, as it is not a simple one-electron  
 230 transfer reaction and deviates from the rule. We ended up a flow cell with  $I^-/I_3^-$  and  $Fe(CN)_6^{3-/4-}$   
 231 chemistry. The reactions below are written in the discharging (galvanic) form below:

- 232 •  $I_3^- + 2e^- \rightarrow 3 I^-$
- 233 •  $Fe(CN)_6^{4-} \rightarrow Fe(CN)_6^{3-} + e^-$

234 The Seebeck coefficients of  $I^-/I_3^-$  and  $Fe(CN)_6^{3-/4-}$  were experimentally determined as +1.04 mV/K and -  
 235 1.40 mV/K, respectively (Fig. S-2a). The values agree with reported values in literature, as the Seebeck  
 236 coefficient of  $Fe(CN)_6^{3-/4-}$  is well documented to be around -1,4 mV/K<sup>27, 28</sup> and  $I^-/I_3^-$  agrees with  
 237 tabulated values when corrected for the concentrations we use here (See SI Note 1). The combination  
 238 of the two electrolytes predicts a cell-Seebeck coefficient of +2.44 mV/K (Fig. 3b).



239 **Figure 3:** **a.** The suggested change in entropy upon valence change of an ion. **b.** Redox potentials as a function of  
 240 temperature for individual redox reactions, obtained via cyclic voltammetry between 20 and 55 °C (Fig. S-2a). To  
 241 avoid temperature changes in the Ag/AgCl reference electrode, a long glass salt bridge was used (Fig. S-8b), **c.**  
 242 and for the assembled RFB cell, at approximately 50% State of Charge (SOC). The slope represents the Seebeck  
 243 coefficients.  
 244

245

246  $K_3Fe(CN)_6$  and  $K_4Fe(CN)_6$  are both soluble up to 0.4 M and have been used in literature at 80 °C,  
247 remaining stable for over 90 days of operation<sup>27, 29</sup>. The polyiodide couple is reported in RFBs well  
248 above 1 M<sup>30</sup> and has a stable cycling performance<sup>31, 32</sup>. Also, triiodide electrolytes have been reported  
249 well over 80 °C<sup>33</sup> and we therefore assumed the redox couple is stable over a large temperature range.

250 As all active species in the selected redox couples are anions, they are separable by a cation exchange  
251 membrane (CEM). The triiodide equilibrium,  $I_3^- \leftrightarrow I_2 + I^-$ , is strongly balanced towards  $I_3^-$ , which  
252 minimizes the potential crossover of  $I_2$ . Also, Ding *et al* have shown that a Nafion membrane could be  
253 used to separate these two electrolytes for 500 cycles with negligible cross-over effects. Moreover,  
254 the combination of these redox couples results in a low cell potential of 0.18 V (at room temperature),  
255 which avoids large energy losses due to self-discharge.

### 256 Single flow cell characterization

257 The OCV of a flow cell exhibits a linear dependence on temperature between 20-40 °C (Fig. 3c),  
258 indicating a constant  $\alpha_{cell}$ . The obtained Seebeck coefficient is +2.88 mV/K, slightly larger than the  
259 individual coefficients that were measured through cyclic voltammetry (+2.44 mV/K). This is likely due  
260 to the different ratio of KI to  $I_2$  in the electrolyte in the flow cell experiments, causing a different Q in  
261 eq. 3 and explaining a change in Seebeck coefficient. The Seebeck coefficient is possibly affected by  
262 the change in reaction entropy to other polyiodides (e.g.  $I_5^-$  or  $I_7^-$ ) that form at higher iodine  
263 concentrations<sup>33</sup> or by the change of reaction towards  $I_2$  instead of  $I_3^-$ , which has a higher Seebeck  
264 coefficient<sup>26</sup>.

265 The area resistance of a single flow cell is 7.1  $\Omega\text{ cm}^2$  at 22 °C and decreases to 3.6  $\Omega\text{ cm}^2$  at 40 °C. We  
266 assume the resistance follows<sup>34</sup>:

$$267 \quad R(T) = \frac{R_0}{1+\theta(T-T_0)} \quad \text{eq. 7}$$

268 Here  $R_0$  (7.1  $\Omega\text{ cm}^2$ ) is the resistance at reference temperature  $T_0$  (22 °C) and  $\theta$  is a fitting parameter  
269 (0.060  $K^{-1}$  for this case, see Fig S-3).

### 270 Comparison with other reported systems

271 We can compare our  $I^-/I_3^- - Fe(CN)_6^{3-/4-}$  system to other thermo-electrochemical systems, by adopting  
272 their dimensionless Figure of Merit (Y). Y is the ratio of available electrical energy to the required  
273 absorbed heat; a higher figure of merit allows one to get a higher heat to power efficiency at a fixed  
274 heat exchanger efficiency. Lee *et al*<sup>11</sup> defined Y as:

$$275 \quad Y = \frac{|\alpha|q_c}{c_p} \quad \text{eq. 8}$$

276 Here  $|\alpha|$  is the absolute Seebeck coefficient of the system,  $q_c$  is the specific charge capacity and  $c_p$  the  
 277 specific heat capacity of the electrodes and electrolyte. Ohmic and Nernstian losses are ignored for all  
 278 systems (see SI Note 4 for more details). Even though other reported TREC systems use solid redox  
 279 species and higher concentrated electrolytes, the system we report here has a comparable figure of  
 280 merit of 0.021 (Table 1), while still having the benefits of liquid handling. A lower Y is expected for all-  
 281 liquid based systems, due to the relatively high heat capacity of water, and poses additional  
 282 requirements for the heat recuperation. However, the concept of redox flow batteries, allowing liquid-  
 283 liquid heat exchangers, easily improves the heat transfer flux by an order of magnitude compared to  
 284 stationary with solid redox species, which justifies the 2-3x lower Y for practical TREC systems.

285 **Table 1.** Comparison with other reported low grade heat TREC systems. The figure of merit Y for our work is  
 286 based on using full range in SOC; smaller  $\Delta$ SOC may be still relevant for a continuous operation with a single  
 287 electrode pair per battery (see **Figure 1D**), and will result in a smaller figure of merit.

Electrolytes	$ \alpha_{\text{cell}} $ (mV/K)	Figure of Merit - Y	System architecture	Ref
$\text{Fe}(\text{CN})_6^{3-/4-}, \text{V}^{3+}/\text{V}^{2+}$	3.00	0.032	Liquid flow cell	18
$\text{VO}_2^+/\text{VO}^{2+}, \text{V}^{3+}/\text{V}^{2+}$	1.16	0.013	Liquid flow cell	17
$\text{Fe}(\text{CN})_6^{3-/4-},$ $\text{Cu}(\text{NH}_3)_4^{2+}/\text{Cu}(\text{NH}_3)_2^+$	2.9	0.033	Liquid stationary cell <sup>a</sup>	25, 35
$\text{CuHCF}, \text{Cu}/\text{Cu}^{2+}$	1.20	0.068	Solid + electrolyte	11, 35
$\text{Fe}(\text{CN})_6^{3-/4-}, \text{FeHCF}$	1.45	0.059	Solid + electrolyte	35, 36
$\text{NiHCF}, \text{Ag}/\text{AgCl}$	0.74	0.034	Solid + supporting electrolyte	13, 35
$\text{Fe}(\text{CN})_6^{3-/4-}, \text{I}^-/\text{I}_3^-$	1.9	0.016	Liquid flow cell	19
$\text{Fe}(\text{CN})_6^{3-/4-}, \text{I}^-/\text{I}_3^-$	2.88	0.021	Liquid flow cell <sup>b</sup>	<i>This work</i>

288 <sup>a</sup> For 0.5 M redox active species. Deposition of  $\text{Cu}_2\text{Fe}(\text{CN})_6$  at the  $\text{BaSO}_4$  precipitate membrane  
 289 prevented continuous operation

290 <sup>b</sup> For 0.3 M redox active species. The maximum solubility allows concentrations up to 0.5 M, which  
 291 would yield  $Y = 0.033$  if the Seebeck coefficient remains the same for this concentration change.

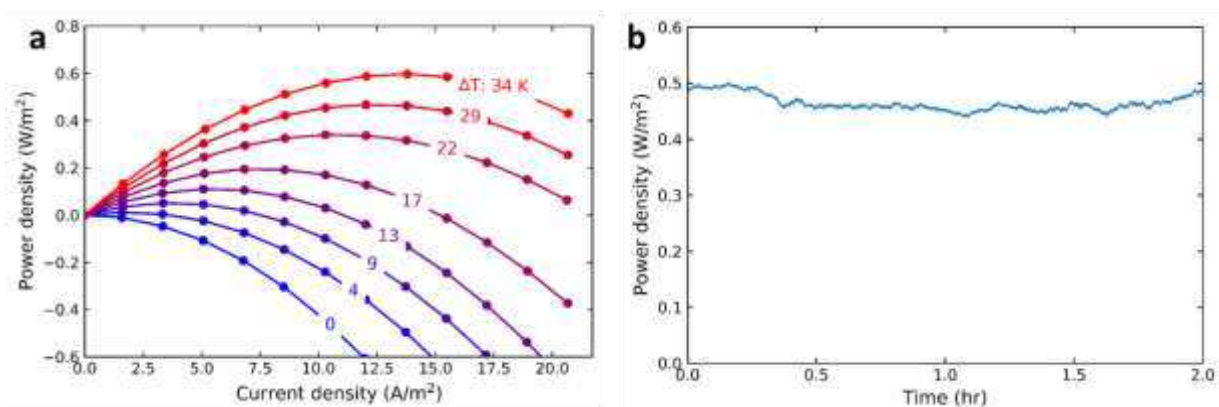
### 293 Proof of concept

294 The heat-to-power performance of the polyiodide/ferrocyanide RFB was evaluated in a continuous  
 295 flow setup with a cold charging and hot discharging flow cell connected in a loop as per Fig. 1a (more  
 296 detailed in Fig. S-4b). Fig. 4a shows the power density versus current densities for various temperature  
 297 differences between the hot and cold cell. We achieved a maximum power density of  $0.6 \text{ W/m}^2$  at  $13.8$   
 298  $\text{A/m}^2$  and a temperature difference of  $34 \text{ }^\circ\text{C}$ . At this current density, the hot and cold cell are cycling  
 299 between a state of charge of 50.0% and 51.2%. The maximum power density shifts to higher current  
 300 densities at higher temperature intervals because both the driving force is larger (larger difference

301  $OCV_{hot} - OCV_{cold}$ ) and the Ohmic resistance is lower at higher temperatures. Still, the optimum current  
302 density is relatively small compared to commercialized RFBs, limiting also the power densities, due to  
303 the high (non-optimized) Ohmic resistance of the system (see Fig. S-3).

304 At the maximum power density in Fig. 4a, 50% of the available energy from the Seebeck effect is  
305 converted into electricity. Here 40% of the energy is lost in Ohmic losses and activation overpotential  
306 and 10% as concentration overpotential. With perfect heat recovery, the present, non-optimized flow  
307 cells would obtain a heat to power efficiency of 5.2% (see SI Note 5 for the derivation). In the present  
308 setup, however, with limited glass heat exchangers (Fig. S-5), and poor insulation of the flow cells and  
309 tubing, an overall heat-to-power efficiency of 0.004% was obtained.

310 The power density of the system, evaluated for 2 hours (Fig. 4b), remained relatively stable around  
311  $0.46 \text{ W/m}^2$ . The fluctuations in the figure are due to small temperature changes and minor changes in  
312 concentration as the electrolyte vessels were not continuously stirred.

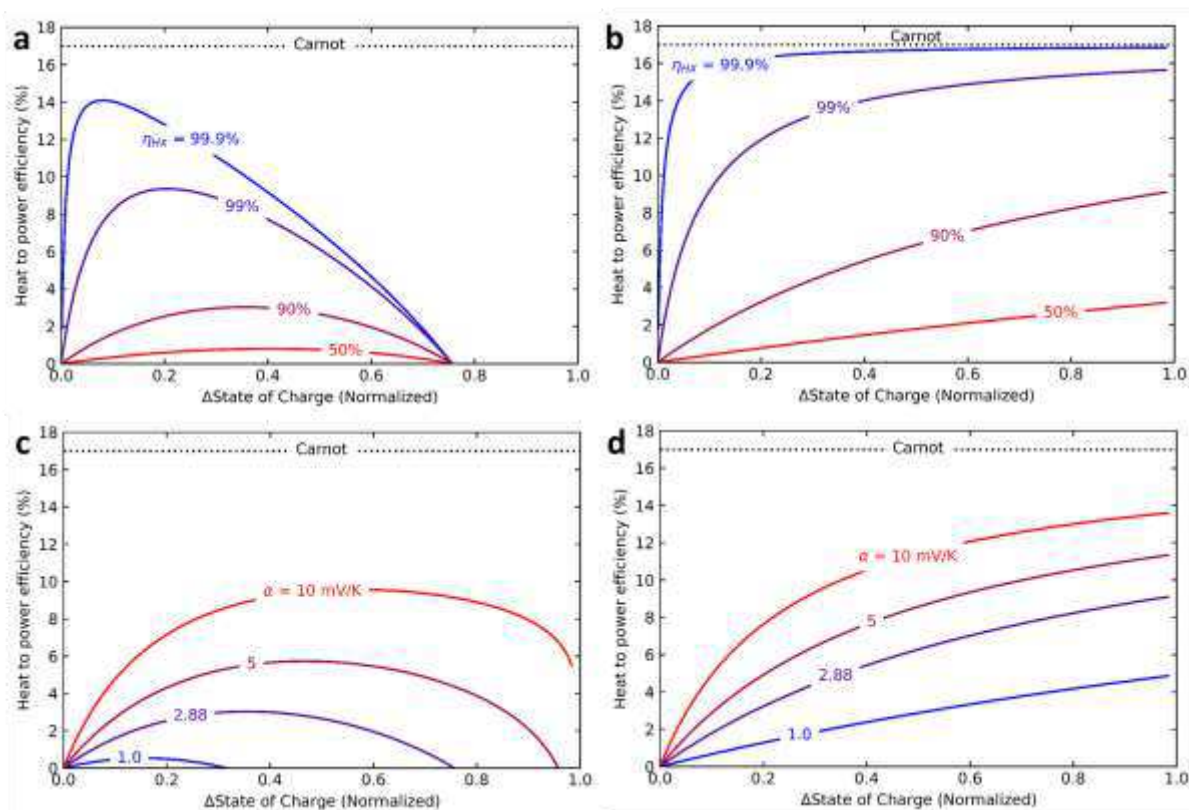


313 **Figure 4:** **a.** Experimental power density as a function of applied current density, for a series of temperature  
314 difference ( $\Delta T$ ) between the hot battery and cold battery. The cold battery temperature is 20 - 22 °C for all  
315 experiments. **b.** Power density of the system over 2 hours, while operating at a  $\Delta T$  of 34 K and 13.4 A/m<sup>2</sup>. The  
316 area (m<sup>2</sup>) in these figures is the electrode area of a single flow cell.  
317

## 318 Outlook

319 Given the early stage of development and the modest power density/energy efficiency, substantial  
320 engineering improvements are necessary to make a RFB based thermo-electrochemical cell feasible  
321 for practical operation. The Seebeck coefficient reduced by 0.21 mV/K after 20 hours of cycling (Fig. S-  
322 6), likely due to I<sub>2</sub> migration across the membrane. We also observed corrosion by iodine and  
323 deposition of Prussian blue on the electrodes and membrane (Fig. S-7). Both the membrane and  
324 electrodes were not selected for long-term stability in this chemistry. Also, our current experimental  
325 design is limited by the high internal resistance and poor insulation.

326 To assess the potential of the reported system we calculated the heat-to-power efficiency of the  
 327 system while varying the  $\Delta$ SOC, heat exchanger efficiency, Seebeck coefficient, heat capacity,  
 328 concentration and Ohmic losses for an optimized system (see SI Note 6). Fig. 5a shows the simulated  
 329 heat-to-power efficiency vs  $\Delta$ SOC for various heat exchanger efficiencies for a RFB system in  
 330 continuous mode. Relying on heat recuperation only, without further improving the Seebeck  
 331 coefficient or cell operation, will be insufficient to reach substantially high energy efficiency in  
 332 continuous flow mode. Even at very high heat exchanger efficiencies (99.9%) a large fraction of energy  
 333 is lost and only a maximum heat to power efficiency of 14% can be obtained. At a more realistic heat  
 334 exchanger efficiency of 90%, only 3% of the waste heat is recovered as electrical power. The maximum  
 335 heat-to-power efficiency shifts to higher  $\Delta$ SOC for lower heat exchanger efficiencies, to reduce the  
 336 amount of fluid that needs to be heated/cooled in poorer heat exchangers. At a  $\Delta$ SOC of 0.75, the  
 337 difference in hot/cold cell voltages becomes 0, due to the hysteresis in the V-dQ curve (Fig. 1d).



338  
 339 *Figure 5: Simulated heat to power efficiency, as a function of width in SOC, in a continuous mode (panel a) and*  
 340 *batch mode (panel b), with hypothetical efficiencies of a heat exchanger. Results in panel a and b are obtained*  
 341 *using  $T_{hot} = 80$  °C,  $T_{cold} = 20$  °C, concentrations for  $Fe(CN)_6^{3-}$ ,  $Fe(CN)_6^{4-}$  and  $I_2$  0.3 M, that of  $I^- = 0.9$  M, and  $\alpha = +2.88$*   
 342 *mV/K. Results in panel c and d are simulated for different Seebeck coefficients at a heat exchanger efficiency of*  
 343 *90%. Ohmic losses are ignored in these calculations.*

344 Fig. 5b shows the heat-to-power efficiency for a system in batch mode. In batch mode the complete  
345 area of the V-dQ curve can be harvested (Fig. 1c), and hence higher efficiencies can be achieved. At a  
346  $\Delta$ SOC of 1 and a perfect heat exchanger the system will approach the Carnot efficiency. Even with a  
347 more realistic heat exchanger efficiency of 90% and  $\Delta$ SOC = 0.5, more than 6% of the heat can be  
348 converted into electricity in batch mode, bettering the current state-of-the-art heat-to-power  
349 technologies. Fig. 5c,d show the effect of the Seebeck coefficient on the heat-to-power efficiency for  
350 a RFB in continuous and batch mode respectively. As the larger Seebeck coefficient increases the  
351 vertical shift of the V-dQ curves, the point of zero work also shifts to higher  $\Delta$ SOC. The Seebeck  
352 coefficient of our system could be increased in practice by the addition a volume fraction of an organic  
353 solvent. The Seebeck coefficient ferro/ferricyanide redox couple has been shown to amplify up to -4,2  
354 mV K<sup>-1</sup> <sup>27, 28</sup> with additives. Preliminary experiments have shown that the addition of ethanol to the  
355 triiodide electrolyte results in a more positive Seebeck coefficient, resulting in a very large cell Seebeck  
356 coefficient (Fig. S-10). The addition of organic solvents does however reduce conductivity and increase  
357 Ohmic losses. Other ways to increase the Seebeck coefficient could be to design a system around  
358 polysulfide (-4.08 to -5.33 mV K<sup>-1</sup>)<sup>37</sup> or a redox reaction with a large  $\Delta$ S due to a phase transition<sup>38, 39</sup>.

359 Finally, the effect of the concentration, heat capacity and Ohmic losses on the heat-to-power efficiency  
360 is assessed (Figures S-8 & S-9). Provided that the heat capacity and maximum concentration have  
361 intrinsic limits, the Ohmic resistance is the only remaining knob for optimizing the heat-to-power  
362 efficiency. A 50 mV Ohmic loss (over the entire two cell circuit) almost halves the heat-to-power  
363 efficiency (at current  $\alpha$ =2.88 mV/K,  $\eta_{\text{HX}}$  = 90%, 0.3 M active species). A zero-gap flow cell design could  
364 be used to minimize the Ohmic resistance and allow for much higher current densities<sup>40</sup>, together with  
365 a low resistive membrane. Hence, this proof of concept of a RFB-based system for continuous heat-to-  
366 power conversion should gain improvement in the realm of higher Seebeck coefficient and low Ohmic  
367 resistances to fully unlock its potential for effective conversion of waste heat to power.

368

369

#### 370 **Data Availability**

371 The data supporting the findings of this study are contained within the paper and its associated  
372 Supplementary Information. All other relevant data is available from the corresponding author upon  
373 reasonable request and in the Zenodo repository at *[to be linked later]*.

374

375

376 **References**

- 377 1. Forman C, Muritala IK, Pardemann R, Meyer B. Estimating the global waste heat potential.  
378 *Renewable and Sustainable Energy Reviews* 2016, **57**: 1568-1579.  
379
- 380 2. IEA (2020) EIO, IEA, Paris <https://www.iea.org/reports/electricity-information-overview>.  
381
- 382 3. Park B-S, Usman M, Imran M, Pesyridis A. Review of Organic Rankine Cycle experimental data  
383 trends. *Energy Conversion and Management* 2018, **173**: 679-691.  
384
- 385 4. Krakhella KW, Bock R, Burheim OS, Seland F, Einarsrud KE. Heat to H2: Using Waste Heat for  
386 Hydrogen Production through Reverse Electrodialysis. *Energies* 2019, **12**(18): 3428.  
387
- 388 5. Tamburini A, Tedesco M, Cipollina A, Micale G, Ciofalo M, Papapetrou M, *et al.* Reverse  
389 electro dialysis heat engine for sustainable power production. *Applied Energy* 2017, **206**:  
390 1334-1353.  
391
- 392 6. Luo X, Cao X, Mo Y, Xiao K, Zhang X, Liang P, *et al.* Power generation by coupling reverse  
393 electro dialysis and ammonium bicarbonate: Implication for recovery of waste heat.  
394 *Electrochemistry Communications* 2012, **19**: 25-28.  
395
- 396 7. Facchinetti I, Cobani E, Brogioli D, La Mantia F, Ruffo R. Thermally Regenerable Redox Flow  
397 Battery. *ChemSusChem* 2020, **13**(20): 5460-5467.  
398
- 399 8. Facchinetti I, Ruffo R, La Mantia F, Brogioli D. Thermally Regenerable Redox Flow Battery for  
400 Exploiting Low-Temperature Heat Sources. *Cell Reports Physical Science* 2020, **1**(5): 100056.  
401
- 402 9. Logan BE, Elimelech M. Membrane-based processes for sustainable power generation using  
403 water. *Nature* 2012, **488**(7411): 313-319.  
404
- 405 10. Lin S, Yip NY, Cath TY, Osuji CO, Elimelech M. Hybrid Pressure Retarded Osmosis–Membrane  
406 Distillation System for Power Generation from Low-Grade Heat: Thermodynamic Analysis  
407 and Energy Efficiency. *Environmental Science & Technology* 2014, **48**(9): 5306-5313.  
408
- 409 11. Lee SW, Yang Y, Lee H-W, Ghasemi H, Kraemer D, Chen G, *et al.* An electrochemical system  
410 for efficiently harvesting low-grade heat energy. *Nature Communications* 2014, **5**(1): 3942.  
411
- 412 12. Abdollahipour A, Sayyaadi H. A review of thermally regenerative electrochemical systems for  
413 power generation and refrigeration applications. *Applied Thermal Engineering* 2021, **187**:  
414 116576.  
415
- 416 13. Yang Y, Loomis J, Ghasemi H, Lee SW, Wang YJ, Cui Y, *et al.* Membrane-Free Battery for  
417 Harvesting Low-Grade Thermal Energy. *Nano Letters* 2014, **14**(11): 6578-6583.  
418
- 419 14. Gao C, Yin Y, Zheng L, Liu Y, Sim S, He Y, *et al.* Engineering the Electrochemical Temperature  
420 Coefficient for Efficient Low-Grade Heat Harvesting. *Advanced Functional Materials* 2018,  
421 **28**(35): 1803129.  
422
- 423 15. Fathabadi H. Internal Combustion Engine Vehicles: Converting the Waste Heat of the Engine  
424 Into Electric Energy to Be Stored in the Battery. *IEEE Transactions on Vehicular Technology*  
425 2018, **67**(10): 9241-9248.  
426

- 427 16. Fathabadi H. Solar energy harvesting in buildings using a proposed novel electrochemical  
428 device as an alternative to PV modules. *Renewable Energy* 2019, **133**: 118-125.  
429
- 430 17. Reynard D, Dennison CR, Battistel A, Girault HH. Efficiency improvement of an all-vanadium  
431 redox flow battery by harvesting low-grade heat. *Journal of Power Sources* 2018, **390**: 30-37.  
432
- 433 18. Poletayev AD, McKay IS, Chueh WC, Majumdar A. Continuous electrochemical heat engines.  
434 *Energy & Environmental Science* 2018, **11**(10): 2964-2971.  
435
- 436 19. Qian X, Shin J, Tu Y, Zhang JH, Chen G. Thermally Regenerative Electrochemically Cycled Flow  
437 Batteries with pH Neutral Electrolytes as for Harvesting Low-Grade Heat. *Physical Chemistry  
438 Chemical Physics* 2021.  
439
- 440 20. deBethune AJ, Licht TS, Swendeman N. The Temperature Coefficients of Electrode Potentials.  
441 *Journal of The Electrochemical Society* 1959, **106**(7): 616.  
442
- 443 21. Elgrishi N, Rountree KJ, McCarthy BD, Rountree ES, Eisenhart TT, Dempsey JL. A Practical  
444 Beginner's Guide to Cyclic Voltammetry. *Journal of Chemical Education* 2018, **95**(2): 197-206.  
445
- 446 22. Blommaert MA, Aili D, Tufa RA, Li Q, Smith WA, Vermaas DA. Insights and Challenges for  
447 Applying Bipolar Membranes in Advanced Electrochemical Energy Systems. *ACS Energy  
448 Letters* 2021: 2539-2548.  
449
- 450 23. Yin S, Zhou L, Du X, Yang Y. Influence of temperature on performance of all vanadium redox  
451 flow battery: analysis of ionic mass transfer. *Ionics* 2019, **25**(2): 593-606.  
452
- 453 24. Li L, Kim S, Wang W, Vijayakumar M, Nie Z, Chen B, *et al.* A Stable Vanadium Redox-Flow  
454 Battery with High Energy Density for Large-Scale Energy Storage. *Advanced Energy Materials*  
455 2011, **1**(3): 394-400.  
456
- 457 25. Hammond RH, Risen WM. An electrochemical heat engine for direct solar energy conversion.  
458 *Solar Energy* 1979, **23**(5): 443-449.  
459
- 460 26. Bratsch S. Standard Electrode Potentials and Temperature Coefficients in Water at 298.15 K.  
461 *Journal of Physical and Chemical Reference Data* 1989, **18**: 1-21.  
462
- 463 27. Inoue D, Fukuzumi Y, Moritomo Y. Volume effect of organic solvent on electrochemical  
464 Seebeck coefficient of  $[\text{Fe}(\text{CN})_6]^{4-}/[\text{Fe}(\text{CN})_6]^{3-}$  in water. *Japanese Journal of Applied Physics*  
465 2020, **59**(3): 037001.  
466
- 467 28. Kim T, Lee JS, Lee G, Yoon H, Yoon J, Kang TJ, *et al.* High thermopower of ferri/ferrocyanide  
468 redox couple in organic-water solutions. *Nano Energy* 2017, **31**: 160-167.  
469
- 470 29. Hu R, Cola BA, Haram N, Barisci JN, Lee S, Stoughton S, *et al.* Harvesting Waste Thermal  
471 Energy Using a Carbon-Nanotube-Based Thermo-Electrochemical Cell. *Nano Letters* 2010,  
472 **10**(3): 838-846.  
473
- 474 30. Weng G-M, Li Z, Cong G, Zhou Y, Lu Y-C. Unlocking the capacity of iodide for high-energy-  
475 density zinc/polyiodide and lithium/polyiodide redox flow batteries. *Energy & Environmental  
476 Science* 2017, **10**(3): 735-741.  
477

- 478 31. Su L, Badel AF, Cao C, Hinricher JJ, Brushett FR. Toward an Inexpensive Aqueous Polysulfide–  
479 Polyiodide Redox Flow Battery. *Industrial & Engineering Chemistry Research* 2017, **56**(35):  
480 9783-9792.  
481
- 482 32. Ding Y, Guo X, Ramirez-Meyers K, Zhou Y, Zhang L, Zhao F, *et al.* Simultaneous energy  
483 harvesting and storage via solar-driven regenerative electrochemical cycles. *Energy &*  
484 *Environmental Science* 2019, **12**(11): 3370-3379.  
485
- 486 33. Palmer DA, Ramette RW, Mesmer RE. Triiodide ion formation equilibrium and activity  
487 coefficients in aqueous solution. *Journal of Solution Chemistry* 1984, **13**(9): 673-683.  
488
- 489 34. Mäntynen M. Temperature correction coefficients of electrical conductivity and of density  
490 measurements for saline groundwater. 2001; 2001.  
491
- 492 35. Gao C, Lee SW, Yang Y. Thermally Regenerative Electrochemical Cycle for Low-Grade Heat  
493 Harvesting. *ACS Energy Letters* 2017, **2**(10): 2326-2334.  
494
- 495 36. Yang Y, Lee SW, Ghasemi H, Loomis J, Li X, Kraemer D, *et al.* Charging-free electrochemical  
496 system for harvesting low-grade thermal energy. *Proceedings of the National Academy of*  
497 *Sciences* 2014, **111**(48): 17011.  
498
- 499 37. Lessner PM, McLarnon FR, Winnick J, Cairns EJ. The Dependence of Aqueous Sulfur-  
500 Polysulfide Redox Potential on Electrolyte Composition and Temperature. *Journal of The*  
501 *Electrochemical Society* 1993, **140**(7): 1847-1849.  
502
- 503 38. Shibata T, Iwaizumi H, Fukuzumi Y, Moritomo Y. Energy harvesting thermocell with use of  
504 phase transition. *Scientific Reports* 2020, **10**(1): 1813.  
505
- 506 39. Yu B, Duan J, Cong H, Xie W, Liu R, Zhuang X, *et al.* Thermosensitive crystallization–boosted  
507 liquid thermocells for low-grade heat harvesting. *Science* 2020, **370**(6514): 342.  
508
- 509 40. Palakkal VM, Nguyen T, Nguyen P, Chernova M, Rubio JE, Venugopalan G, *et al.* High Power  
510 Thermally Regenerative Ammonia-Copper Redox Flow Battery Enabled by a Zero Gap Cell  
511 Design, Low-Resistant Membranes, and Electrode Coatings. *ACS Applied Energy Materials*  
512 2020, **3**(5): 4787-4798.  
513

514

## 515 Acknowledgements

516 The authors thank Christiaan Schinkel, Evert Wagner, Duco Bosma and Stefan ten Hagen (TU Delft)  
517 for their valuable technical support.

518 This project has received funding from the European Research Council  
519 (ERC) under the European Union’s Horizon 2020 research and innovation  
520 programme (grant agreement No 852115). This work reflects the  
521 authors' view and the ERC Executive Agency is not responsible for any  
522 use resulting from the information it contains.  
523



524

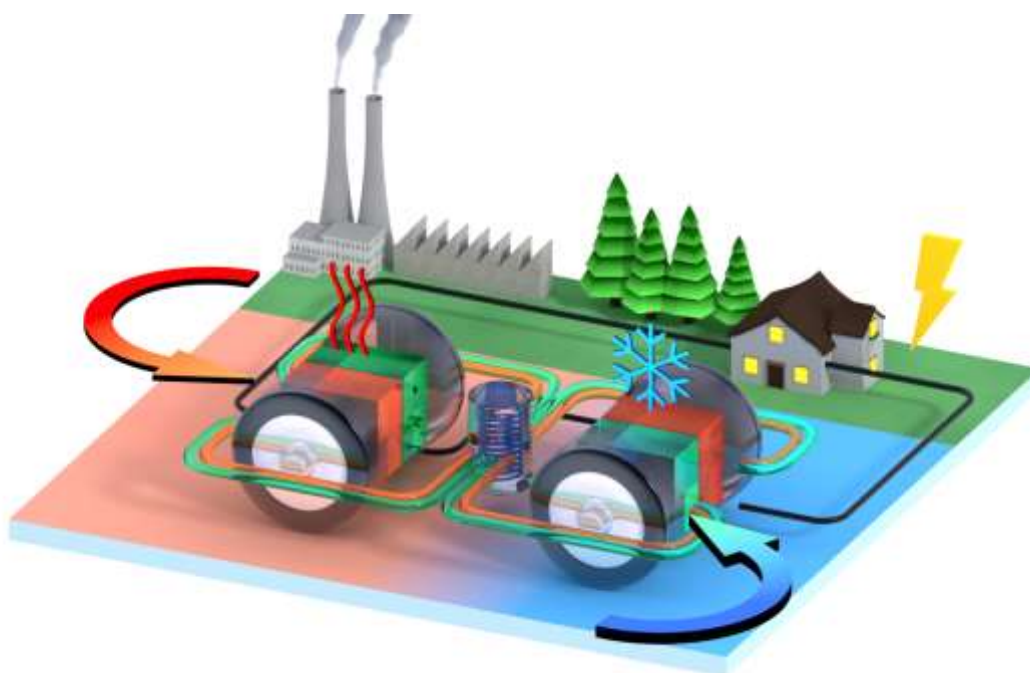
525 **Author contributions**

526 J.B. and D.V. chose the electrolytes and designed the first system. J.B. and S.R. characterized the  
527 electrolytes and performed the heat-to-power experiments and analysed the data. J.B. performed  
528 the Python calculations. D.V. and J.V. had the initial idea for using RFBs in heat-to-power. D.V.  
529 supervised the project and acquired funding. J.B. and D.V. wrote the paper. All the authors discussed  
530 and contributed to the writing.

531

532

533 **Graphical abstract**



534

## Supplementary Files

This is a list of supplementary files associated with this preprint. Click to download.

- [SIThermoelectrochemicalflowcell.docx](#)